

Three-dimensional mapping and electronic origin of large altermagnetic splitting near Fermi level in CrSb

Guowei Yang^{*1}, Zhanghuan Li^{†2}, Sai Yang³, Jiyuan Li³, Hao Zheng¹, Weifan Zhu¹, Saizheng Cao¹, Wenxuan Zhao⁴, Jiawen Zhang¹, Mao Ye⁵, Yu Song¹, Lun-Hui Hu¹, Lexian Yang⁴, Ming Shi¹, Huiqiu Yuan^{1,6}, Yongjun Zhang^{‡3}, Yuanfeng Xu^{§1} and Yang Liu^{¶1,6}

¹*Center for Correlated Matter and School of Physics, Zhejiang University, Hangzhou 310058, China*

²*Beijing National Laboratory for Condensed Matter Physics, Institute of Physics, Chinese Academy of Sciences, Beijing 100190, China*

³*Hubei Key Laboratory of Photoelectric Materials and Devices, School of Materials Science and Engineering, Hubei Normal University, Huangshi 435002, China*

⁴*State Key Laboratory of Low Dimensional Quantum Physics, Department of Physics, Tsinghua University, Beijing 100084, China*

⁵*Shanghai Synchrotron Radiation Facility, Shanghai Advanced Research Institute, Chinese Academy of Sciences, Shanghai 201204, China*

⁶*Collaborative Innovation Center of Advanced Microstructures, Nanjing University, Nanjing 210093, China*

Abstract

Recently, a new kind of collinear magnetism, dubbed altermagnetism, has attracted considerable interests. A key characteristic of altermagnet is the momentum-dependent band and spin splitting without net magnetization. However, finding altermagnetic materials with large splitting near the Fermi level, which necessarily requires three-dimensional k -space mapping and is crucial for spintronic applications and emergent phenomena, remains challenging. Here by employing synchrotron-based angle-resolved photoemission spectroscopy (ARPES) and model calculations, we uncover a large altermagnetic splitting, up to ~ 1.0 eV, near the Fermi level in CrSb. We verify its bulk-type g -wave altermagnetism through systematic three-dimensional k -space mapping, which unambiguously reveals the altermagnetic symmetry and associated nodal planes. The ARPES results are well captured by density functional theory calculations. In addition, tight-binding model analysis indicate that the large altermagnetic splitting arises from strong third-nearest-neighbor hopping mediated by Sb ions, which breaks both the space-time reversal symmetry and the translational spin-rotation symmetry. The large band/spin splitting near Fermi level in metallic CrSb, together with its high T_N (up to 705 K) and simple spin configuration, paves the way for exploring emergent phenomena and spintronic applications based on altermagnets.

^{*}These authors contributed equally to this paper

[†]These authors contributed equally to this paper

[‡]yjzhang@hbnu.edu.cn

[§]y.xu@zju.edu.cn

[¶]yangliuphys@zju.edu.cn

Introduction

Despite intensive research over the years, magnetism has remained one of the most vibrant areas in physics research. Even the commensurate collinear magnetic order, which seems to be the simplest case, is no exception. Besides the well-studied ferromagnetism and antiferromagnetism, a new type of collinear magnetism, dubbed altermagnetism, has been proposed theoretically [1–10] and verified experimentally in MnTe [11–16]. There have also been experimental evidences supporting the altermagnetism in RuO₂ [17–22], although the nature of magnetism in RuO₂ remains debated [23]. Altermagnet is often defined in the absence of spin-orbit coupling (SOC) and can be classified by the spin space group, different from ferromagnet and conventional antiferromagnet. Although altermagnets exhibit zero net magnetization in real space, they have spin-split electronic bands in reciprocal space. While the zero bulk magnetization allows for ultrafast manipulation with low stray field, akin to an antiferromagnet, the time-reversal symmetry breaking and momentum-dependent spin polarization in altermagnets can give rise to emergent properties useful for device applications, such as anomalous Hall effects [16–18, 24, 25], giant/tunneling magnetoresistance [26, 27], spin current, spin-torque effects [19–21, 28–30], spin caloritronics (Nernst effect) [31–33]. In addition, unconventional superconductivity based on altermagnetic materials has been theoretically proposed [34–38], making them a fertile playground for exploring novel superconducting states. The momentum-dependent spin splitting has also been found recently in the noncoplanar system MnTe₂ [39], which significantly expands the scope of altermagnetic materials.

The characteristic momentum-dependent spin splitting in an altermagnet lies in its special spin-group symmetry, i.e., the opposite-spin sublattices are connected by a real-space rotation or mirror operation, instead of a translation or inversion. Depending on the dimensionality and lattice/spin symmetry, altermagnets can be classified into planar-type or bulk-type with *d*-, *g*- or *i*-wave symmetry [8], corresponding to two, four or six spin-degenerate nodal planes crossing the Γ point, respectively. Since the nodal planes often coincide with high-symmetry momentum planes, it is important to investigate the altermagnetic splitting in three-dimensional momentum space. While altermagnetic splittings have been observed experimentally in MnTe, how the altermagnetic splitting evolves in three-dimensional momentum space remains unexplored. The dependence with respect to out-of-plane and in-plane momenta is important to understand the nature of altermagnetism. Most importantly, for enhanced physical properties and real applications, it is critical to find strong altermagnets with large band/spin splittings near the Fermi level (E_F) and with magnetic ordering temperature well above room temperature.

Here in this paper, we present direct spectroscopic evidence of the largest altermagnetic band splitting reported so far, up to \sim 1.0 eV near E_F in CrSb, from synchrotron-based angle-resolved photoemission spectroscopy (ARPES) measurements combined with ab initio calculations and tight-binding (TB) model analysis. CrSb is traditionally known for its itinerant antiferromagnetism with a high Néel temperature up to 705 K [40]. Although altermagnetic band splitting was recently reported in (100)-oriented CrSb films by soft X-ray ARPES [41], high-resolution three-dimensional k -space mapping of the altermagnetic splitting, which is key to confirm (and understand) the altermagnetism proposed in CrSb [8], is still lacking. Our high-resolution ARPES data from (001)-oriented single crystals unambiguously reveal the characteristic k_z and in-plane momentum dependence of the altermagnetic splitting in CrSb. The ARPES results are in good agreement with the ab initio calculations from density functional theory (DFT). We further demonstrate through TB model analysis that the large altermagnetic splitting stems from the strong third-nearest-neighbor hoppings of Cr 3d orbitals mediated by the Sb 5p orbitals, which break both the space-time reversal symmetry and the translational spin-rotation symmetry. Such insight can be important for designing and tuning altermagnetic materials with desirable properties.

Results

Sample characterization and lattice/spin structure.

CrSb crystallizes in the hexagonal NiAs-type structure. As shown in Fig. 1a, each Cr atom is coordinated to the top and bottom Sb triangles with AB stacking, forming a tilted octahedron. The sharp X-ray diffraction (XRD) pattern from a (001)-oriented crystal, shown in Fig. 1b, confirms the high crystal quality with the extracted lattice constants of $a = b = 4.12 \text{ \AA}$, $c = 5.44 \text{ \AA}$, close to the previously reported value of $a = 4.12 \text{ \AA}$ and $c = 5.47 \text{ \AA}$ [40]. The magnetic structure of CrSb, confirmed by a number of studies based on neutron scattering [42–45], belongs to the magnetic space group $P6'_3/m'm'c$, where the magnetic moments of Cr (aligned along the [001] axis) are parallel within the hexagonal Cr layer and antiparallel between two neighboring layers. Ignoring the SOC, which is weak for Cr 3d electrons and plays a minor role in the low-energy band structure (see below), the altermagnetism in CrSb can be well defined and characterized by non-relativistic spin-group symmetries. As defined in [8, 9, 46–50], a spin space group operation is a combination of spin rotation operation and real-space transformation, namely $[R_i^s \parallel R_j]$, where R_i^s acts only in spin space (containing only identity transformation E and spin-flip operation C_2^s for collinear magnetic systems), while R_j operates in real space. The two opposite-spin sublattices in altermagnets should be connected by a (screw) n -fold rotation (C_n) or (glide) mirror (M) symmetry in real space, rather than by translation (\vec{t}) or inversion (P) symmetry. As illustrated in Fig. 1c, the two Cr sublattices with opposite spins in CrSb are related by a spin group symmetry $[C_2^s \parallel M_z]$ or $[C_2^s \parallel \tilde{C}_{6z}]$, where \tilde{C}_{6z} is a six-fold rotation along z axis combined with a translation $\vec{t} = (0, 0, \frac{1}{2})c$. Both the spin group symmetries $[C_2^s \parallel \vec{t}]$ and $[T \parallel P]$ (space-time reversal) are broken in CrSb, resulting in momentum-dependent spin splitting in the electronic band structure. As shown in Fig. 1d, on the mirror invariant planes, i.e. the horizontal planes at $k_z = 0$ and $0.5c^*$ ($c^* = 2\pi/c$), and three equivalent vertical planes containing $\bar{K} - \bar{\Gamma} - \bar{K}$ related to C_{3z} , the spin splitting is zero. Therefore, CrSb can be classified as a three-dimensional (or bulk-type) g -wave altermagnet with four nodal planes crossing the Γ point [8].

The in-plane k_x - k_y map from ARPES measurements using 200 eV photons is shown in Fig. 1e, which shows (hole-like) pockets centered at $\bar{\Gamma}$ with the in-plane periodicity consistent with the (001) surface. The k_z dispersion of the valence bands along $\bar{\Gamma} - \bar{M}$, obtained from the photon-energy-dependent scan, is shown in Fig. 1f. The observed periodic modulation of the bands with the photon energy allows us to determine the inner potential V_0 to be $\sim 17 \text{ eV}$ (see also Fig. 2), which is used to convert the photon energy to k_z , as shown in Fig. 1f. Note that here the k_z band dispersion is directly related to bulk-type altermagnetic band splitting, according to Fig. 1d. In the ab initio calculations, we find that the altermagnetic splitting in CrSb is maximized along the in-plane $\bar{\Gamma} - \bar{M}$ direction at $k_z \sim 0.25c^*$, with a magnitude of $\sim 1.0 \text{ eV}$.

The k_z dependence of bulk-type altermagnetic splitting.

The k_z -dependent band splitting indicates the bulk-type altermagnetism in CrSb. In Figs. 2a-c, we show the valence bands taken with three representative photon energies (80, 68, and 90 eV) along the $\bar{\Gamma} - \bar{M}$ direction (more data are included in Fig. S8 in [51]). For the 80 eV photons (corresponding to $k_z \sim 0.28c^*$) in Fig. 2a, two sets of hole bands centered at $\bar{\Gamma}$ can be observed with an energy splitting up to 1.0 eV near E_F . By contrast, only one hole band can be observed near E_F under 68 eV (Fig. 2b, $k_z \sim 0$) and 90 eV (Fig. 2c, $k_z \sim 0.5c^*$) photons. The valence bands can be better visualized by taking the second derivatives, as shown in Figs. 2d-f. Such a k_z -dependent band splitting is consistent with the expected altermagnetic splitting illustrated in Fig. 1d. To make quantitative comparison, we performed ab initio calculations from DFT incorporating both the altermagnetism and SOC (AM with SOC), as shown in Figs. 2g-i. The calculations can well reproduce the experimental band structure, including the hole-type valence bands near E_F and a bundle of bands from -1 eV to -3 eV. Most importantly, the observed k_z -dependent splitting near

E_F shows good agreement with the ab initio results, as indicated by the green arrows in Figs. 2d,g. The calculations further show that the valence bands at the $k_z = 0$ and $k_z = 0.5c^*$ planes have zero spin polarization (black color), while the split valence bands at $k_z = 0.28c^*$ exhibit strong spin polarization (red and blue colors).

The altermagnetic order is essential for the observed band splitting, while the SOC plays a minor role. To see this, we present DFT calculations at $k_z = 0.28c^*$ without considering altermagnetism [nonmagnetic (NM) with SOC, Fig. 2j] or SOC (AM without SOC, Fig. 2k). Comparing Figs. 2j,k with Fig. 2g, it is clear that the altermagnetism is critical to yield the observed band structure, while the influence from SOC over the band dispersion is much weaker.

In general, spin is a good quantum number in altermagnets. When SOC comes into play, the SU(2) symmetry is broken and the bands with opposite spins will couple to each other. Nevertheless, in CrSb, the bands crossing E_F are mainly contributed by the 3d orbitals on Cr, which have weak SOC. It is therefore natural to expect that SOC has only small impact over the band structure near E_F (comparing Figs. 2g,k). By calculating the expectation value of \hat{S}_z , as shown in Fig. 2g, we find that the spin quantum number can still be approximated as a half-integer ($\pm\frac{1}{2}$).

The k_x - k_z map at $E = -0.5$ eV with fine k_z steps is shown in Fig. 2l; the corresponding constant-energy contour from DFT calculations is displayed in Fig. 2m. The experimental results and DFT calculations agree quite well: the altermagnetic splitting is close to zero at $k_z = 0$ and gradually increases to its maximal value at $k_z \sim 0.25c^*$ (black arrows in Figs. 2l,m), eventually decreasing to zero at $k_z = 0.5c^*$. Such a k_z dependence unambiguously confirms the bulk-type altermagnetic splitting in CrSb.

The in-plane symmetry of g -wave altermagnetism.

The in-plane momentum dependence of the band splitting provides direct evidence for the g -wave altermagnetism in CrSb. Figs. 3a,b show the k_x - k_y maps at two representative energies taken with 80 eV photons ($k_z \sim 0.28c^*$), where the flower-like hole-type pockets centered at $\bar{\Gamma}$ can be observed. The constant-energy contours from ab initio calculations are overlaid on top in Figs. 3a,b, which agree well with the experimental data. Based on the spin group symmetry analysis, the spin-resolved contours have three-fold rotational symmetry, and the bands with different spin are related by a 60° rotation, leading to the observed six-fold flower-like pockets in the spin-integrated ARPES (Figs. 3a,b). Fig. 3c shows energy-momentum cuts at a series of representative θ angles, where θ is the azimuthal angle between the momentum \mathbf{k} and the $\bar{\Gamma} - \bar{K}$ direction, defined in Fig. 3b. The results clearly demonstrate the presence (absence) of altermagnetic band splitting along $\bar{\Gamma} - \bar{M}$ ($\bar{\Gamma} - \bar{K}$), as well as the gradual evolution of the splitting between these two directions. These experimental results are consistent with the corresponding spin-resolved band structures from ab initio calculations in Fig. 3d (see Fig. S9 in [51] for more details).

To quantitatively analyze the in-plane dependence of altermagnetic splitting, we also extract the momentum distribution curves (MDCs) at $E = -0.6$ eV from Fig. 3c and plot them in Fig. 3e. The MDCs are then fitted with two Gaussian peaks (see Fig. S10 in [51] for details) to yield the momentum splitting (Δk) as a function of θ (Fig. 3f). The momentum splitting agrees well with the ab initio calculation (see also Fig. S10 in [51]), including the $|\sin(3\theta)|$ -like functional form and the magnitude of splitting, although small deviations are likely present due to the experimental uncertainty or inaccuracy in theoretical calculations. We mention that the bulk-type g -wave altermagnetism only requires a six-fold in-plane symmetry in the magnitude of the band splitting, although the exact location of the nodal planes (along either $\bar{\Gamma} - \bar{K}$ or $\bar{\Gamma} - \bar{M}$) is still dependent on the details of the lattice [8].

Mechanism behind the large altermagnetic splitting.

Although the altermagnetic band splitting can be characterized by its corresponding spin group symmetry, its amplitude is dependent on the chemical bonding strength in real material. In this

section, we construct a microscopic TB model to delve into the mechanism behind the large altermagnetic splitting in CrSb. Based on orbital analysis of the electronic band structure of CrSb, we find that the set of bands intersecting E_F is primarily contributed by the d_{xz} , d_{yz} , d_{xy} , and $d_{x^2-y^2}$ orbitals on Cr, which are hybridized with the p orbitals on Sb (Details can be found in Section 1 of [51]). It is important to note that both (d_{xz}, d_{yz}) and $(d_{xy}, d_{x^2-y^2})$ share the same symmetry property (the irreducible representation E_g) under the site symmetry of Cr (point group D_{3d}). Therefore, one E_g per Cr atom is sufficient to construct the effective model. A comprehensive derivation of the TB model is provided in Section 1 of [51]. Ignoring SOC, the model can be formally expressed as follows,

$$H(\mathbf{k}) = \begin{bmatrix} H^\uparrow(\mathbf{k}) & 0_{4 \times 4} \\ 0_{4 \times 4} & H^\downarrow(\mathbf{k}) \end{bmatrix} = \sum_{i=0,3} \sum_{j,m=0,1,2,3} f_{ijm}(\mathbf{k}) \Gamma_{ijm} \quad (1)$$

where $\Gamma_{ijm} = s_i \otimes \sigma_j \otimes \tau_m \equiv s_i \sigma_j \tau_m$. The Pauli matrices $s_{i=0,1,2,3}$ (or σ_i or τ_i) are used here to represent the space of spin (or the two sublattices Cr₁ and Cr₂ or the two orbitals ϕ_1 and ϕ_2 about E_g).

By incorporating all the spin group symmetries and considering the kinetic hopping terms up to the 3NN sites, we have found that both the NN and the NNN hopping terms preserve the translational spin-flip operation $[C_2^s \parallel \vec{t}]$ [51]. It indicates that neither the NN nor the NNN hopping results in an altermagnetic spin splitting (see Fig. 1a for illustration of NN, NNN and 3NN hoppings). It is only when we take into consideration the 3NN terms that the altermagnetic splitting occurs. As demonstrated in [51], there are five 3NN terms in Eq. 1, i.e. Γ_{011} , Γ_{013} , Γ_{010} , Γ_{311} and Γ_{313} , and their coefficients are

$$\begin{aligned} f_{011}(\mathbf{k}) &= 2\sqrt{3}(q_4 - q_1) \sin^2\left(\frac{k_1}{2}\right) \cos\left(\frac{k_3}{2}\right), \\ f_{013}(\mathbf{k}) &= 2(q_4 - q_1) \sin^2\left(\frac{k_1}{2}\right) \cos\left(\frac{k_3}{2}\right), \\ f'_{010}(\mathbf{k}) &= 2(q_1 + q_4) \cos\left(\frac{k_3}{2}\right) [2 \cos(k_1) + 1], \\ f_{311}(\mathbf{k}) &= 3(q_2 + q_3) \sin(k_1) \sin\left(\frac{k_3}{2}\right), \\ f_{313}(\mathbf{k}) &= \sqrt{3}(q_2 + q_3) \sin(k_1) \sin\left(\frac{k_3}{2}\right), \end{aligned} \quad (2)$$

where q_i 's ($i = 1, 2, 3, 4$) are the independent 3NN hopping parameters between Cr atoms at $R_1 = (0, 0, 0)$ and $R_2 = (1, 1, \frac{1}{2})$, as defined below [51]

$$\begin{aligned} q_1 &= \langle \phi_1, Cr_1, R_1 | \hat{H} | \phi_1, Cr_2, R_2 \rangle, \\ q_2 &= \langle \phi_1, Cr_1, R_1 | \hat{H} | \phi_2, Cr_2, R_2 \rangle, \\ q_3 &= \langle \phi_2, Cr_1, R_1 | \hat{H} | \phi_1, Cr_2, R_2 \rangle, \\ q_4 &= \langle \phi_2, Cr_1, R_1 | \hat{H} | \phi_2, Cr_2, R_2 \rangle. \end{aligned} \quad (3)$$

The first three 3NN terms in Eq. 2, i.e., $f_{011}(\mathbf{k})\Gamma_{011}$, $f_{013}(\mathbf{k})\Gamma_{013}$ and $f'_{010}(\mathbf{k})\Gamma_{010}$, preserve the $[C_2^s \parallel \vec{t}]$ symmetry, and they do not give rise to any altermagnetic splitting. In contrast, the last two 3NN terms $f_{311}(\mathbf{k})\Gamma_{311}$ and $f_{313}(\mathbf{k})\Gamma_{313}$, which are proportional to $q_2 + q_3$, break both $[T \parallel P]$ and $[C_2^s \parallel \vec{t}]$ symmetries, leading to the altermagnetic band/spin splitting.

By fitting the band structure from DFT calculations, especially along the $\bar{\Gamma} - \bar{M}$ direction near E_F , we obtain all the free parameters used in the TB model (the resulting band dispersion of the TB model is shown in Fig. 4b). We find that the fitted 3NN hopping parameters, especially $q_2 + q_3$

that gives rise to the spin splitting, are of the similar magnitude as the NNN hoppings (see Table 2 in [51]), which is counterintuitive. Indeed, d orbitals are usually very local, and the direct 3NN hopping should be very small. This is further confirmed by the DFT calculations, as shown in Table 1. In the section 2 of [51], our additional analysis based on the Wannier calculations show that the strong 3NN hoppings are dominated by a second-order hopping process mediated by Sb. In other words, the p orbitals on Sb assist the 3NN hopping between d orbitals on Cr. As tabulated in Table 1, the amplitude of $q_2 + q_3$ that arises from the direct and assistant hopping processes are about 21 and 152 meV, respectively. Their total contribution is indeed very close to the one used in the TB model. Therefore, the Sb ions between the two Cr sublattices play a crucial role for the surprisingly large 3NN hopping and hence the strong altermagnetic splitting in CrSb. Our model analysis suggest that the altermagnetic splitting in CrSb can be tuned by pressure or strain, which can strongly modify the hopping processes assisted by Sb ions.

Table 1: Values of the 3NN hopping parameters. The parameters in the second row are the ones used in the fitted eight-band TB model. The parameters in the third and fourth rows indicate contributions of the direct hopping (DH) and assistant hopping (AH) processes obtained from DFT calculations. The last row is the total hopping (TH) after summation of the direct and assistant hoppings. The energy unit is eV.

Parameter	q_1	$q_2 + q_3$	q_4
TB	-0.0184	0.1950	0.1942
DFT(DH)	0.0050	0.0214	-0.0660
DFT(AH)	-0.0234	0.1516	0.2602
DFT(TH)	-0.0184	0.1730	0.1942

In Fig. 4c, by changing the values of $q_2 + q_3$ and $q_1 + q_4$, we further investigate the evolution of the altermagnetic energy splitting ΔE_U at the momentum point U , i.e., the midpoint between $\bar{\Gamma}$ and \bar{M} in the $k_z = 0.28$ c^* plane, where the energy splitting is close to the maximal value. Our results show that the altermagnetic splitting depends sensitively on the magnitude of $q_2 + q_3$: the splitting ΔE_U is exactly zero when $q_2 + q_3$ is zero, and ΔE_U increases almost linearly with $q_2 + q_3$ in a large parameter space, where the 3NN hopping dominates the altermagnetic splitting. On the other hand, the values of q_1 and q_4 affect ΔE_U appreciably only when $q_2 + q_3$ is larger than ~ 0.2 eV, where hoppings beyond 3NN become appreciable. Figure 4d shows the evolution of the altermagnetic energy splitting ΔE along $\bar{\Gamma} - \bar{M}$, by increasing the numerical values of $\{q_i\}$ while keeping a fixed ratio among them (corresponding to the grey dashed line in Fig. 4c). These calculations, which can simulate the process of uniform compression, indicate a clear increase in the magnitude of altermagnetic splitting under hydrostatic pressure.

Discussion

It is interesting to compare CrSb with MnTe, another bulk-type g -wave altermagnet with similar crystal structure [12]. There are several important differences between these two systems. Firstly, the $3d$ spins in CrSb are aligned along the c axis, in contrast to the in-plane $3d$ spins in MnTe. This eliminates multiple band splittings caused by the different in-plane domains as reported in MnTe [12, 14, 52] and allows for clear identification of altermagnetic splitting in CrSb. Secondly, the valences of Cr and Mn should be different, leading to different fillings of the $3d$ valence bands and hence distinct ground states (metallic in CrSb and semiconducting in MnTe). Finally, the lattice constant c in CrSb (5.44 Å) is considerably smaller than that of MnTe (6.75 Å), which, together

with the stronger electron correlation in MnTe with $U \sim 4.8$ eV [12], gives rise to stronger electron hopping and hence larger altermagnetic splitting up to 1.0 eV near E_F in CrSb. By contrast, the observed altermagnetic splitting in MnTe is $\lesssim 0.5$ eV and is located far below E_F [11, 12].

The mechanism of large altermagnetic splitting in CrSb can be further illustrated by comparison with VNb_3S_6 , which is another proposed bulk-type g -wave altermagnet with the identical spin group symmetry as CrSb and MnTe [9]. Yet its much larger lattice constant $c = 12.17$ Å [53] and weak interlayer coupling between the V and NbS_2 layers result in a very small splitting of a few tens of meV (see Fig. S11 in [51]). The large difference of the splitting magnitude in CrSb and VNb_3S_6 highlights the important role of interlayer electron hopping (the 3NN hopping in this case), which is mediated by coupling with the nonmagnetic ions, as discussed above.

The large bulk-type g -wave altermagnetic splitting at E_F in CrSb provides interesting opportunities to explore novel superconducting proximity effects at the interfaces between metallic altermagnets and conventional superconductors. For instance, it has been theoretically proposed that the interface between a conventional superconductor and a planar d -wave altermagnet can induce finite-momentum pairing [36], and their planar Josephson junctions can exhibit orientation-dependent $0\text{-}\pi$ oscillations [37]. In contrast, due to the three-dimensional spin-degenerate nodal planes of CrSb, both planar and vertical Josephson junctions composed of CrSb could exhibit similar (or even richer) superconducting properties. For example, the vertical Josephson junction could achieve damped oscillating pairing along any direction non-parallel to the nodal planes, facilitating the toggling of finite-momentum pairing on and off by controlling the orientation of the interface. Therefore, our work will motivate future theoretical and experimental studies to explore such intriguing phenomena.

In summary, we present direct spectroscopic evidence of bulk-type g -wave altermagnetism in CrSb from high-resolution three-dimensional k -space mapping obtained by synchrotron-based ARPES measurements. Our systematic k_z and in-plane momentum dependent study confirms a large altermagnetic splitting up to 1.0 eV near E_F , which is in good agreement with the DFT calculations. Our TB model analysis reveals that the altermagnetic splitting arises mainly from the 3NN hopping of Cr 3d electrons mediated by Sb 5p orbitals, highlighting the important role of electronic coupling between magnetic and nonmagnetic ions. The insight can be important for finding/tuning altermagnetic materials with enhanced properties. The large altermagnetic splitting near E_F , together with the high ordering temperature up to 700 K in CrSb, paves the way for exploring emergent phenomena and practical applications based on altermagnets.

Methods

Single crystal growth and characterizations.

Single crystals of CrSb were grown using an antimony flux. The elements were combined in a molar ratio of Cr:Sb of 2:3, and sealed in an evacuated quartz tube. The tube was heated up to 1150 °C and held at this temperature for 20 hours, before being cooled down slowly to 700 °C and centrifuged to remove the excess antimony flux. The lateral size of the single crystals is typically 1x1 mm². The chemical composition of the crystals was confirmed by energy dispersive X-ray spectroscopy. The crystal structure was checked by XRD measurements (Fig. 1b and Fig. S5b in [51]). The temperature-dependent resistivity was measured using a Physical Property Measurement System (PPMS), and it shows metallic behavior with no phase transition from 300 K down to 1.8 K (Fig. S5a in [51]), consistent with previous reports [54]. The cleaved single crystals were also characterized by core-level photoemission measurements, which show expected core level peaks from Cr 3p and Sb 4d electrons (Fig. S5c in [51]), without any trace of impurities.

Synchrotron-based ARPES measurements. The ARPES measurements were carried out at the BLOCH beamline in Max IV Lab (Sweden) and the BL03U beamline at Shanghai Synchrotron

Radiation Facility (SSRF, China). The typical energy resolution was set to \sim 20 meV and the measurement temperature is \sim 20 K. The typical beam spot is \sim 15 \times 15 μm^2 for the BLOCH beamline and \sim 50 \times 50 μm^2 for the BL03U beamline. The ARPES measurements were performed on the (001)-oriented surface, which was cleaved *in situ* at measurement temperature and under ultrahigh vacuum ($< 5 \times 10^{-11}$ mbar). All ARPES data in our manuscript were taken with horizontally polarized photons.

Ab initio calculations. The DFT calculations were performed using the Vienna Ab initio Simulation Package (VASP) [55, 56]. The Perdew, Burke and Ernzerhoff (PBE) parametrization of generalized gradient approximation (GGA) to the exchange-correlation functional was employed [57]. We performed calculations with different choices of the coulomb repulsion U (see Fig. S6 in [51]), and we found that $U = 0$ shows the best agreement with the experimental results. Therefore, U is set to zero in all calculations, unless noted otherwise. An energy cutoff of 345 eV and $11 \times 1 \times 9$ Γ -centered K-mesh were employed to converge the total energy to 1 meV/atom. The band structure obtained from PBE method were fitted to a tight-binding model Hamiltonian with maximally projected Wannier function method, which was then used to calculate the Fermi surface with wannier_tools package. To understand the underlying origin of altermagnetic splitting, calculations with either SOC or AM turned off, i.e., AM without SOC or NM with SOC, were both performed (see Fig. S7 in [51]). The results show that altermagnetism plays a dominant role in the observed band structure, while the SOC effect is not very important.

Acknowledgments This work is supported by the National Key R&D Program of China (Grant No. 2023YFA1406303, No. 2022YFA1402200), the Key R&D Program of Zhejiang Province, China (2021C01002), the National Natural Science Foundation of China (No. 12174331, No. 12204159, No. 12374163, No. 12350710785) and the State Key project of Zhejiang Province (No. LZ22A040007). We acknowledge MAX IV Laboratory for time on Beamline BLOCH under Proposal 20230343. Research conducted at MAX IV, a Swedish national user facility, is supported by the Swedish Research council under contract 2018-07152, the Swedish Governmental Agency for Innovation Systems under contract 2018-04969, and Formas under contract 2019-02496. Part of this research used beamline 03U of the Shanghai Synchrotron Radiation Facility, which is supported by the ME2 project under Contract No. 11227902 from the National Natural Science Foundation of China. We would like to thank Prof. Dawei Shen, Dr. Zhengtai Liu, Dr. Balasubramanian Thiagarajan and Dr. Mats Leandersson for experimental help. We are also grateful to Prof. Yulin Chen, Prof. Chang Liu, Mr. Qi Jiang and Prof. Xin Lu for useful discussions. Some of the images in the paper were created using VESTA software [58].

Author contributions The project was designed by Y. L. Single crystal growth and characterization was done by S. Y., J. L., J. Z., H. Y. and Y. Z, with help from S. C., and Y. S. The ARPES measurement was performed by G. Y., with help from H. Z., W. Z., W. X., M. Y., L. Y., M. S. and Y. L. ARPES data analysis was done by G. Y. and Y. L., with help from Z. L. and Y. X. Ab initio calculations and tight-binding model analysis were carried out by Z. L. and Y. X. L.-H. H. contribute to the discussion. The manuscript was prepared by G. Y., Z. L., Y. X. and Y. L., with inputs from all other coauthors. All authors discussed the results and commented on the manuscript.

Competing interests The authors declare no competing interests.

Additional information Supplementary Information is available for this paper.

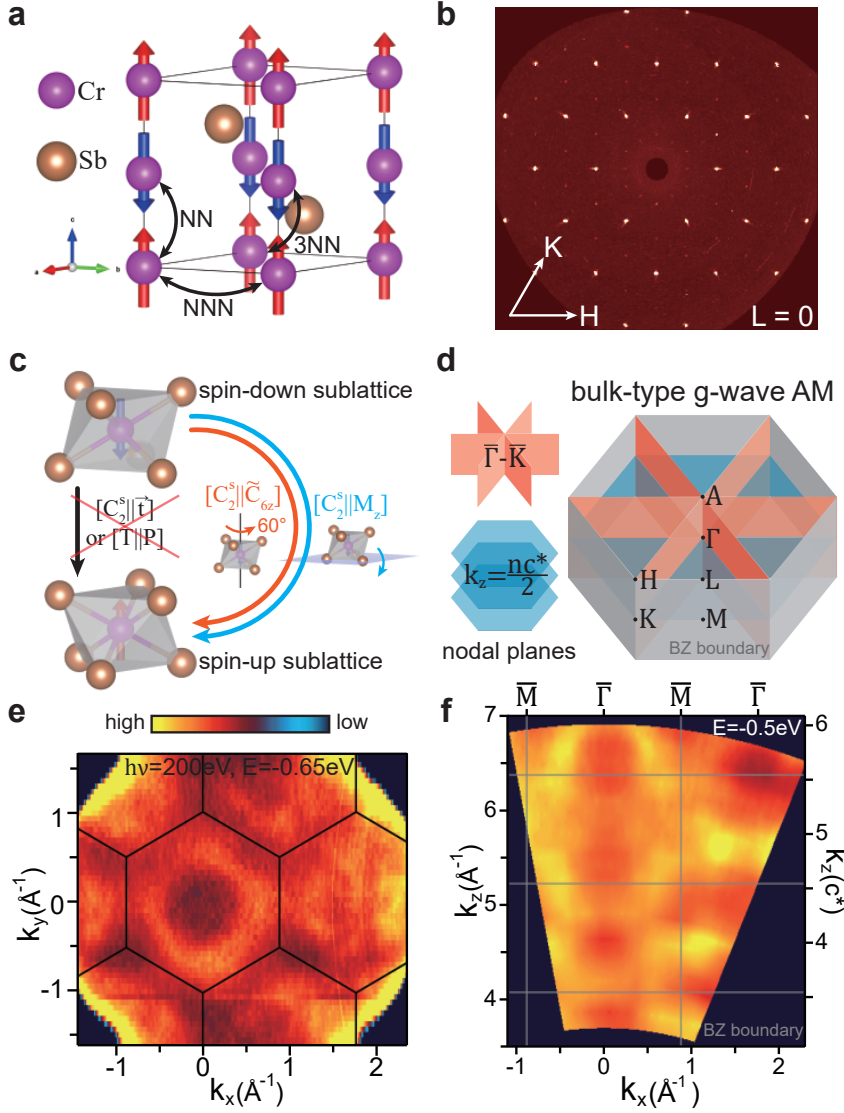


Fig. 1: Spin/lattice structure and characterization of CrSb. **a** Spin and lattice structure of CrSb. The nearest neighbor (NN), next nearest neighbor (NNN), and third nearest neighbor (3NN) Cr-Cr bonds are indicated by the black arrow lines. **b** H-K map ($L = 0$) of a (001)-oriented crystal from XRD. **c** Symmetry operations connecting the opposite-spin sublattices. **d** Left: the nodal planes corresponding to spin-group symmetries in (c). Right: The BZ with high symmetry points and nodal planes labelled. **e** The in-plane k_x - k_y map at $E = -0.65$ eV, taken with 200 eV photons (corresponding to $k_z \sim 0.5c^*$). **f** The k_x - k_z map at $E = -0.5$ eV along $\bar{\Gamma}-\bar{M}$ (k_x). The black hexagons in (e) and grey rectangles in (f) mark the Brillouin zone (BZ) boundaries. The color bar for image plots in (e,f) is indicated.

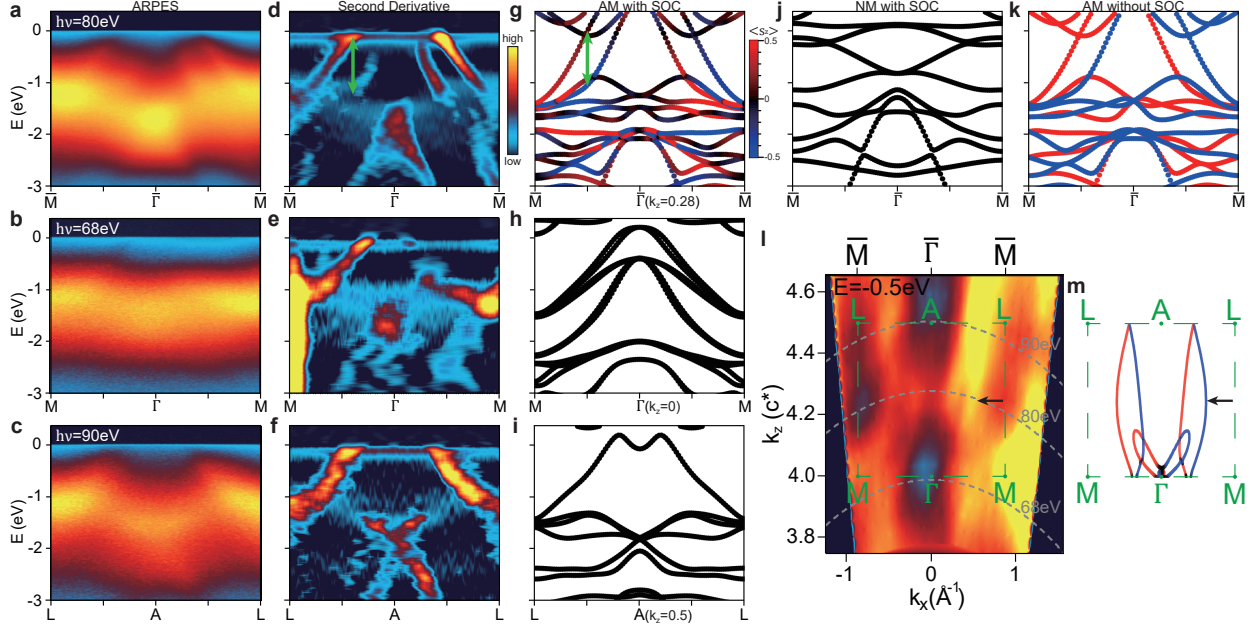


Fig. 2: The k_z dependence of altermagnetic splittings along the in-plane $\bar{\Gamma} - \bar{M}$ direction. **a,b,c** ARPES spectra taken with 80 eV (a), 68 eV (b), 90 eV (c) photons. **d,e,f** The second derivatives of the ARPES spectra corresponding to (a-c). **g,h,i** Spin-resolved band structure from DFT calculations considering both AM and SOC at $k_z = 0.28c^*$ (g), 0 (h) and $0.5c^*$ (i), for comparison with experimental data on the left. The green arrows in (d,g) highlight the altermagnetic band splittings. **j,k** DFT calculations at $k_z = 0.28c^*$, considering only SOC (j, NM with SOC) or altermagnetism (k, AM without SOC), for comparison with (g). **l** The k_x - k_z map at $E = -0.5$ eV. The green dashed rectangle marks half of the BZ from $M - \Gamma - M$ ($k_z = 0$) to $L - A - L$ ($k_z = 0.5c^*$). Grey dashed curves indicate the k_x - k_z cuts corresponding to (a-c). **m** The k_x - k_z contour at $E = -0.5$ eV from DFT, for comparison with (l). Black arrows in (l,m) mark the altermagnetic splitting maximized near $k_z = 0.25c^*$. The colors of the curves in (g-k,m) indicate the spin polarization [color bar in (g)].

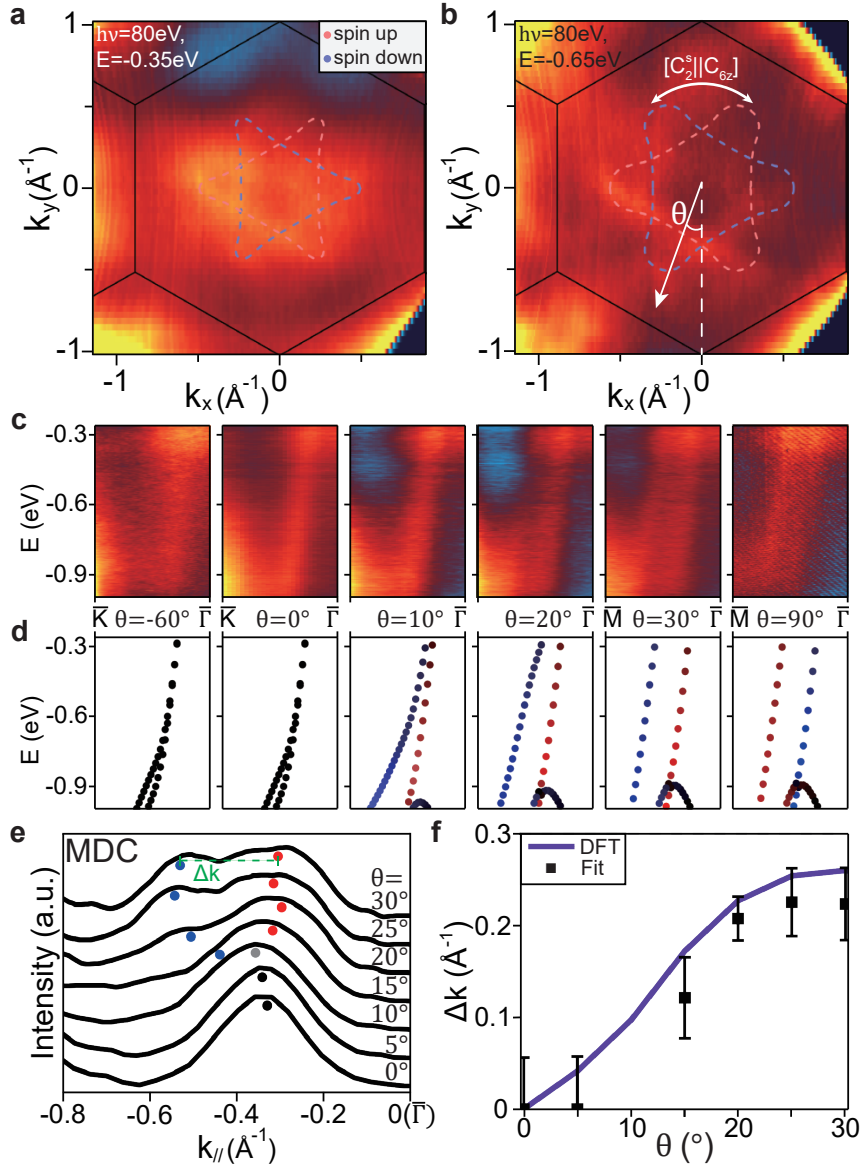


Fig. 3: The in-plane altermagnetic splitting at $k_z \sim 0.28c^*$. **a,b** The experimental k_x - k_y map at $E = -0.35$ eV (**a**) and -0.65 eV (**b**), taken with 80 eV photons and using the deflection mode. The corresponding constant-energy contours from DFT calculations are overlaid on top as dashed curves. **c** The energy-momentum cuts for a few representative θ values (defined in [**b**]). **d** Band structure from DFT for comparison with (**c**). The momentum range for each plot in (**c,d**) is from the BZ boundary (left) to $\bar{\Gamma}$. The curve colors in (**a,b,d**) indicate the spin polarization. **e** MDCs at $E = -0.6$ eV for θ from 0° to 30° . Dots indicate fitted peak positions. **f** The extracted altermagnetic momentum splitting Δk (black boxes with error bars) from (**e**), in comparison with DFT calculation (purple curve).

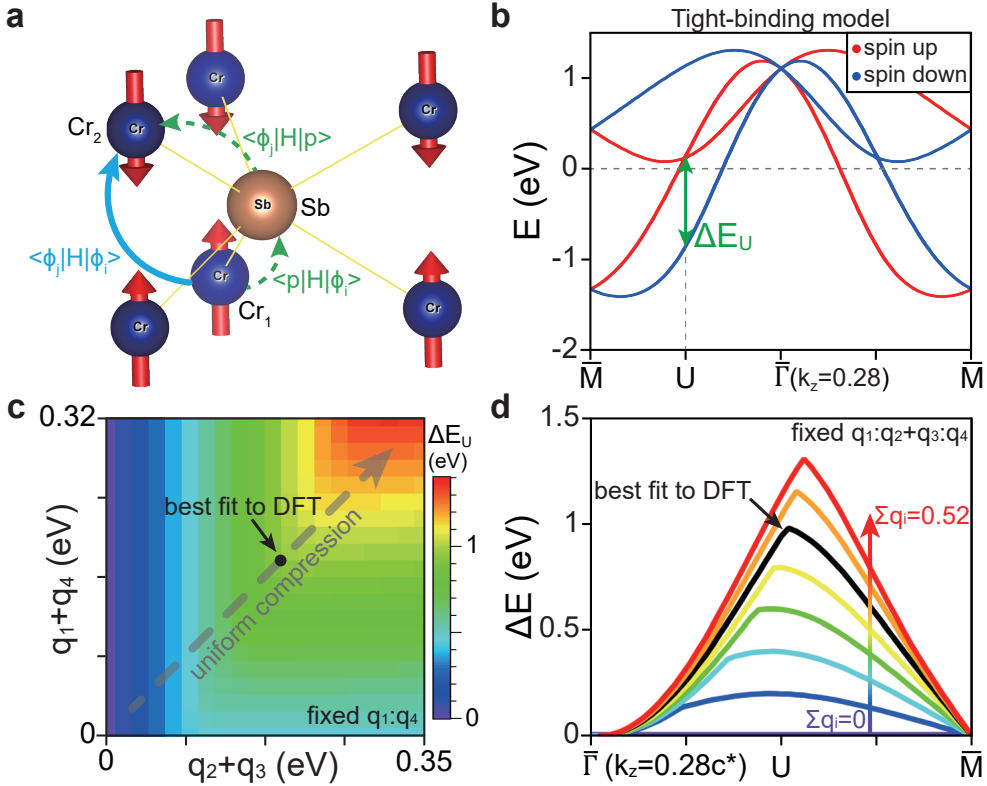


Fig. 4: Origin of the large altermagnetic splitting in CrSb. **a** The dominant hopping process between the 3NN Cr atoms at $R_1 = (0, 0, 0)$ (Cr₁) and $R_2 = (1, 1, \frac{1}{2})$ (Cr₂), which is mediated by the p orbitals on the Sb atom at $(\frac{1}{3}, \frac{2}{3}, \frac{1}{4})$. Here we use Cr₁ (Cr₂) to present the Cr sublattice with positive (negative) spins. **b** Band dispersion along the $\bar{\Gamma}-\bar{M}$ direction at $k_z = 0.28c^*$ obtained from the eight-band TB model. The red and blue lines represent spin-up and spin-down bands, respectively. **c** Altermagnetic band splittings at the U point (the midpoint between $\bar{\Gamma}$ and \bar{M} in the $k_z = 0.28c^*$ plane) as a function of $q_2 + q_3$ and $q_1 + q_4$. The color bar for the image plot is shown on the right. The black dot corresponds to the parameters obtained through best fit to DFT calculations ($q_1 = -0.0184$, $q_4 = 0.1942$, $q_2 + q_3 = 0.1950$). **d** Altermagnetic band splittings along the $\bar{\Gamma}-\bar{M}$ direction at $k_z = 0.28c^*$ by increasing the value of $\sum q_i$ from 0 to 0.52 eV, where the ratio $q_1 : q_2 + q_3 : q_4$ is fixed. The black curve corresponds to the best fit with DFT calculations.

References

- [1] Wu, C., Sun, K., Fradkin, E. & Zhang, S.-C. Fermi liquid instabilities in the spin channel. *Phys. Rev. B* **75**, 115103 (2007).
- [2] Hayami, S., Yanagi, Y. & Kusunose, H. Momentum-dependent spin splitting by collinear antiferromagnetic ordering. *Journal of the Physical Society of Japan* **88**, 123702 (2019).
- [3] Šmejkal, L., Gonzalez-Hernandez, R., Jungwirth, T. & Sinova, J. Crystal time-reversal symmetry breaking and spontaneous Hall effect in collinear antiferromagnets. *Sci Adv* **6**, eaaz8809 (2020).
- [4] Hayami, S., Yanagi, Y. & Kusunose, H. Spontaneous antisymmetric spin splitting in non-collinear antiferromagnets without spin-orbit coupling. *Phys. Rev. B* **101**, 220403 (2020).
- [5] Yuan, L.-D., Wang, Z., Luo, J.-W., Rashba, E. I. & Zunger, A. Giant momentum-dependent spin splitting in centrosymmetric low-Z antiferromagnets. *Phys. Rev. B* **102**, 014422 (2020).
- [6] Mazin, I. I., Koepernik, K., Johannes, M. D., González-Hernández, R. & Šmejkal, L. Prediction of unconventional magnetism in doped FeSb₂. *Proceedings of the National Academy of Sciences* **118**, e2108924118 (2021).
- [7] Liu, P., Li, J., Han, J., Wan, X. & Liu, Q. Spin-group symmetry in magnetic materials with negligible spin-orbit coupling. *Phys. Rev. X* **12**, 021016 (2022).
- [8] Šmejkal, L., Sinova, J. & Jungwirth, T. Beyond conventional ferromagnetism and antiferromagnetism: A phase with nonrelativistic spin and crystal rotation symmetry. *Phys. Rev. X* **12**, 031042 (2022).
- [9] Šmejkal, L., Sinova, J. & Jungwirth, T. Emerging research landscape of altermagnetism. *Phys. Rev. X* **12**, 040501 (2022).
- [10] Šmejkal, L., MacDonald, A. H., Sinova, J., Nakatsuji, S. & Jungwirth, T. Anomalous Hall antiferromagnets. *Nature Reviews Materials* **7**, 482 (2022).
- [11] Lee, S. *et al.* Broken Kramers degeneracy in altermagnetic MnTe. *Phys. Rev. Lett.* **132**, 036702 (2024).
- [12] Krempaský, J. *et al.* Altermagnetic lifting of Kramers spin degeneracy. *Nature* **626**, 517–522 (2024).
- [13] Osumi, T. *et al.* Observation of a giant band splitting in altermagnetic MnTe. *Phys. Rev. B* **109**, 115102 (2024).
- [14] Hajlaoui, M. *et al.* Temperature dependence of relativistic valence band splitting induced by an altermagnetic phase transition. Preprint at <https://arxiv.org/abs/2401.09187> (2024).
- [15] Hariki, A. *et al.* X-ray magnetic circular dichroism in altermagnetic α -MnTe. *Phys. Rev. Lett.* **132**, 176701 (2024).
- [16] Gonzalez Betancourt, R. D. *et al.* Spontaneous anomalous Hall effect arising from an unconventional compensated magnetic phase in a semiconductor. *Phys. Rev. Lett.* **130**, 036702 (2023).
- [17] Feng, Z. *et al.* An anomalous Hall effect in altermagnetic ruthenium dioxide. *Nature Electronics* **5**, 735–743 (2022).

- [18] Tschirner, T. *et al.* Saturation of the anomalous Hall effect at high magnetic fields in altermagnetic RuO₂. *APL Materials* **11**, 101103 (2023).
- [19] Bose, A. *et al.* Tilted spin current generated by the collinear antiferromagnet ruthenium dioxide. *Nature Electronics* **5**, 267–274 (2022).
- [20] Bai, H. *et al.* Observation of spin splitting torque in a collinear antiferromagnet RuO₂. *Phys. Rev. Lett.* **128**, 197202 (2022).
- [21] Karube, S. *et al.* Observation of spin-splitter torque in collinear antiferromagnetic RuO₂. *Phys. Rev. Lett.* **129**, 137201 (2022).
- [22] Fedchenko, O. *et al.* Observation of time-reversal symmetry breaking in the band structure of altermagnetic RuO₂. *Science Advances* **10**, eadj4883 (2024).
- [23] Hiraishi, M. *et al.* Nonmagnetic ground state in RuO₂ revealed by muon spin rotation. *Phys. Rev. Lett.* **132**, 166702 (2024).
- [24] Wang, M. *et al.* Emergent zero-field anomalous Hall effect in a reconstructed rutile antiferromagnetic metal. *Nature Communications* **14**, 8240 (2023).
- [25] Leiviskä, M. *et al.* Anisotropy of the anomalous hall effect in the altermagnet candidate Mn₅Si₃ films. Preprint at <https://arxiv.org/abs/2401.02275v1> (2024).
- [26] Šmejkal, L., Hellenes, A. B., González-Hernández, R., Sinova, J. & Jungwirth, T. Giant and tunneling magnetoresistance in unconventional collinear antiferromagnets with nonrelativistic spin-momentum coupling. *Phys. Rev. X* **12**, 011028 (2022).
- [27] Cui, Q., Zhu, Y., Yao, X., Cui, P. & Yang, H. Giant spin-Hall and tunneling magnetoresistance effects based on a two-dimensional nonrelativistic antiferromagnetic metal. *Phys. Rev. B* **108**, 024410 (2023).
- [28] Gonzalez-Hernandez, R. *et al.* Efficient electrical spin splitter based on nonrelativistic collinear antiferromagnetism. *Phys. Rev. Lett.* **126**, 127701 (2021).
- [29] Bai, H. *et al.* Efficient spin-to-charge conversion via altermagnetic spin splitting effect in antiferromagnet RuO₂. *Phys. Rev. Lett.* **130**, 216701 (2023).
- [30] Shao, D.-F. *et al.* Néel spin currents in antiferromagnets. *Phys. Rev. Lett.* **130**, 216702 (2023).
- [31] Zhou, X. *et al.* Crystal thermal transport in altermagnetic RuO₂. *Phys. Rev. Lett.* **132**, 056701 (2024).
- [32] Badura, A. *et al.* Observation of the anomalous Nernst effect in altermagnetic candidate Mn₅Si₃. Preprint at <https://arxiv.org/abs/2403.12929> (2024).
- [33] Han, L. *et al.* Observation of non-volatile anomalous Nernst effect in altermagnet with collinear Néel vector. Preprint at <https://arxiv.org/abs/2403.13427> (2024).
- [34] Zhu, D., Zhuang, Z.-Y., Wu, Z. & Yan, Z. Topological superconductivity in two-dimensional altermagnetic metals. *Phys. Rev. B* **108**, 184505 (2023).
- [35] Brekke, B., Brataas, A. & Sudbø, A. Two-dimensional altermagnets: Superconductivity in a minimal microscopic model. *Phys. Rev. B* **108**, 224421 (2023).
- [36] Zhang, S.-B., Hu, L.-H. & Neupert, T. Finite-momentum Cooper pairing in proximitized altermagnets. *Nature Communications* **15**, 1801 (2024).

- [37] Ouassou, J. A., Brataas, A. & Linder, J. dc Josephson effect in altermagnets. *Phys. Rev. Lett.* **131**, 076003 (2023).
- [38] Xu, C. *et al.* Frustrated altermagnetism and charge density wave in kagome superconductor CsCr_3Sb_5 films. Preprint at <https://arxiv.org/abs/2309.14812> (2023).
- [39] Zhu, Y.-P. *et al.* Observation of plaid-like spin splitting in a noncoplanar antiferromagnet. *Nature* **626**, 523–528 (2024).
- [40] Takei, W. J., Cox, D. E. & Shirane, G. Magnetic structures in the MnSb-CrSb system. *Physical Review* **129**, 2008–2018 (1963).
- [41] Reimers, S. *et al.* Direct observation of altermagnetic band splitting in CrSb thin films. *Nature Communications* **15**, 2116 (2024).
- [42] Snow, A. I. Neutron diffraction investigation of the atomic magnetic moment orientation in the antiferromagnetic compound CrSb. *Phys. Rev.* **85**, 365–365 (1952).
- [43] Takei, W. J., Cox, D. E. & Shirane, G. Magnetic structures in the MnSb-CrSb system. *Phys. Rev.* **129**, 2008–2018 (1963).
- [44] Abe, S., Kaneko, T., Ohashi, M., Yoshida, H. & Kamigaki, K. Magnetic properties of CrSb. *Journal of the Physical Society of Japan* **53**, 2703–2709 (1984).
- [45] Yuan, J., Song, Y., Xing, X. & Chen, J. Magnetic structure and uniaxial negative thermal expansion in antiferromagnetic CrSb. *Dalton Trans.* **49**, 17605 (2020).
- [46] Brinkman, W. F., Elliott, R. J. & Peierls, R. E. Theory of spin-space groups. *Proceedings of the Royal Society of London. Series A. Mathematical and Physical Sciences* **294**, 343–358 (1966).
- [47] Litvin, D. & Opechowski, W. Spin groups. *Physica* **76**, 538–554 (1974).
- [48] Xiao, Z., Zhao, J., Li, Y., Shindou, R. & Song, Z.-D. Spin space groups: Full classification and applications. Preprint at <https://arxiv.org/abs/2307.10364> (2023).
- [49] Ren, J. *et al.* Enumeration and representation of spin space groups. Preprint at <https://arxiv.org/abs/2307.10369> (2023).
- [50] Jiang, Y. *et al.* Enumeration of spin-space groups: Towards a complete description of symmetries of magnetic orders. Preprint at <https://arxiv.org/abs/2307.10371> (2023).
- [51] See online Supplementary Information.
- [52] Mazin, I. I. Altermagnetism in mnte: Origin, predicted manifestations, and routes to detwinning. *Phys. Rev. B* **107**, L100418 (2023).
- [53] Lu, K. *et al.* Canted antiferromagnetic order in the monoaxial chiral magnets $\text{V}_{1/3}\text{TaS}_2$ and $\text{V}_{1/3}\text{NbS}_2$. *Phys. Rev. Mater.* **4**, 054416 (2020).
- [54] Suzuoka, T. An electrical resistance study of the system $(\text{Cr}_x\text{Mn}_{1-x})\text{Sb}$. *Journal of the Physical Society of Japan* **12**, 1344–1347 (1957).
- [55] Kresse, G. & Hafner, J. Ab initio molecular dynamics for liquid metals. *Phys. Rev. B* **47**, 558–561 (1993).

- [56] Kresse, G. & Joubert, D. From ultrasoft pseudopotentials to the projector augmented-wave method. *Phys. Rev. B* **59**, 1758–1775 (1999).
- [57] Perdew, J. P., Burke, K. & Ernzerhof, M. Generalized gradient approximation made simple. *Phys. Rev. Lett.* **77**, 3865–3868 (1996).
- [58] Momma, K. & Izumi, F. *VESTA3* for three-dimensional visualization of crystal, volumetric and morphology data. *Journal of Applied Crystallography* **44**, 1272–1276 (2011).